Experiments in Fluids 22 (1997) 447–457 © Springer-Verlag 1997

On the evolution of laminar vortex rings

A. Weigand, M. Gharib

Abstract Using Laser Doppler Anemometry (LDA) and Digital Particle Image Velocimetry (DPIV), the physical properties of laminar vortex rings are investigated in the Reynolds-number range $830 \leqslant Re \leqslant 1650$. The measured initial circulations of the vortex rings are found to agree well with corrected versions of the vorticity-flux (slug-flow) model proposed by Didden and Pullin. The DPIV and LDA data show excellent agreement regarding local velocities and vortex-ring circulations. The DPIV data depict the distribution of the vorticity and circulation in the core regions, where the resulting vorticity distributions are found to be self-similar Gaussian profiles. The propagation velocity of the vortex rings is well approximated by an analytical model of Saffman for large core sizes. In the asymptotic limit $t \rightarrow \infty$, the trajectories are in excellent agreement with the exact Stokes-dipole solution of Cantwell and Rott.

1
Introduction

Vortex rings are one of the simplest forms of three-dimensional vortex flows and have been subject to many studies in the past. Shariff and Leonard (1992) provide a comprehensive review on the formation, evolution, and structure of vortex rings. However, the unsteady nature of vortex-rings makes it difficult to map the velocity and vorticity fields by means of single-point measurement techniques (e.g., hot-wire or Laser Doppler Anemometry). In this regard, the scope of available experimental data is limited and insufficient to resolve questions such as the distribution of vorticity and circulation in the core region and the decay of the propagation speed of vortex rings.

Our interest in vortex rings grew mainly out of the need to establish a flow standard for investigations of vortex-ring/boundary interactions such as the interaction with solid walls (Weigand 1993) and free surfaces (Gharib et al. 1992; Gharib and Weigand 1996). The present work focuses on the measurement of the circulation, vorticity distribution in the core region, and spatio-temporal evolution of laminar vortex rings in a Reynolds-number range of $830 \leqslant Re \leqslant 1650$ (The Reynolds number is defined by the ratio of the circulation to the kinematic viscosity). Six different flow cases were investigated using flow visualization, Laser Doppler Anemometry (LDA), and the whole field velocity-measurement technique Digital Particle Image Velocimetry (DPIV). These combined studies made it possible to compare the obtained results with various analytical models and previous investigations where only flow visualization or single-point measurement techniques have been used.

Didden (1979), Glezer and Coles (1990), and Nitsche and Krasny (1994) provide valuable information on the formation process of laminar vortex rings. In our studies, we examine correction formulas for the initial circulation suggested by the experimental results of Didden and the similarity arguments of Pullin (1979). The resulting velocity and vorticity fields of the different flow cases are compared to single-point LDA measurements and to models of vorticity distributions suggested by Widnall et al. (1974) and Maxworthy (1977).

Reynolds-number effects on the evolution of the trajectory of vortex rings have been experimentally studied by Maxworthy (1972) and Sallet and Widmayer (1974). The exact analytical solution for the asymptotic drift velocity of vortex rings by Cantwell and Rott (1988) and the numerical calculations of Stanaway et al. (1988) have renewed the importance of Saffman's (1970) analytical models for the trajectory of thin- and thick-cored vortex rings. In the present study, we pay special attention to Saffman's models and their accuracy in predicting the trajectory and the asymptotic decay of vortex rings.

2
Experimental set-up and procedures

Figure 1 shows a general schematic of the experimental setup. Experiments were conducted in a water tank using a mechanical vortex-ring generator. Vortex rings of diameter D, circulation Γ, and propagation velocity U_V are generated by a piston that pushes fluid out of a sharp-edged cylindrical nozzle into the surrounding. The x-axis coincides with the center-line of the vortex-ring generator, and the nozzle-exit plane is located in the plane $x = 0$.

Received: *11 October 1995*/*Accepted*: *22 March 1996*

A. Weigand, M. Gharib
California Institute of Technology,
Graduate Aeronautical Laboratories, 205-45
Pasadena, CA 91125, USA

Correspondence to: A. Weigand

The support of the Office of Naval Research (ONR-URI grant N00014-92-J-1610) under the program management of Dr. Edwin Rood is gratefully acknowledged.

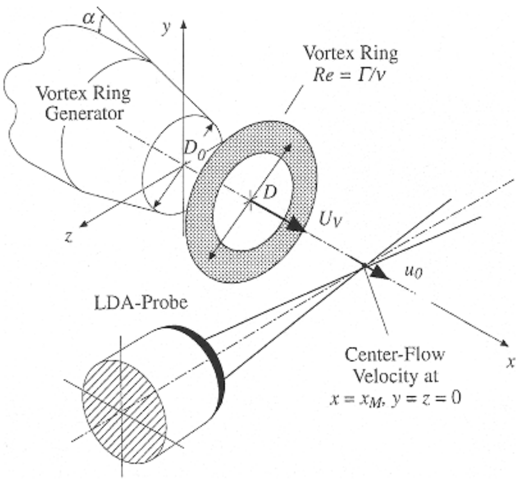

Fig. 1. General schematic of experimental setup and Laser Doppler Anemometry (LDA)

The cylindrical nozzle has an inner orifice diameter of $D_0 = 3.0$ cm, and its outer contour is wedge-shaped with a tip angle of $\alpha = 20°$. The 20°-wedge extends 2.0 cm upstream of the nozzle-exit plane. A computer-controlled micro-stepping motor drives a linear traverse mechanism and controls the motion profile of the piston, while an inductive Linear Variable Displacement Transducer (LVDT) monitors the actual piston displacement. The mechanical design limits the maximum stroke of the piston to $(L/D_0)_{\max} = 0.87$ and the maximum acceleration and deceleration to $|a|_{\max} \approx 450$ cm/s^2.

The computer control provides precise timing and synchronization of different events (time resolution better than 10^{-3} s). These events include vortex-ring generation, dye injection for flow visualization, and initialization of measurement processes such as Laser Doppler Anemometry (LDA) and Digital Particle Image Velocimetry (DPIV).

Various flow-visualization techniques, all using dye as a fluid marker, were applied to make the vortex ring visible. For example, the initial vortex-ring fluid volume that is displaced by the piston is marked by filling the cylinder volume of the generator with dye. The initial roll up of the vortex sheet is visualized by releasing a small amount of dye out of a thin circumferential slot at the tip of the nozzle.

As Fig. 1 shows, single-point LDA measurements with titanium-dioxide (TiO_2) particles as seeding material (average diameter of 0.5 μm) were primarily conducted to determine the temporal evolution of center-flow velocities $u_0 = u_0(t)$ at various distances x_M downstream of the nozzle-exit plane.

Figure 2a shows a schematic of the experimental setup for DPIV measurements. The flow is seeded with neutrally buoyant, silver-coated glass spheres (average diameter of 14 ± 5 μm) and illuminated by a sheet of laser light with a thickness of approximately 0.1 cm. The video camera is positioned normal to the measurement plane and records an image sequence of particle fields with a spatial resolution of 768 × 480 pixels. As Figs. 2a and b show, the exposure times $t_{e,1}$, $t_{e,2}$, and the time difference Δt between two successive exposures are synchronized and controlled by a camera controller and shutter in order to prevent streaking particle images and to limit the maximum displacement of particles. In the DPIV measurements presented here, the exposure times and the time difference between exposures were set to $t_{e,1} = t_{e,2} = 4 \cdot 10^{-3}$ s and $\Delta t = 8 \times 10^{-3}$ s, respectively. Using a window size of 32 × 32 pixels and a step size for the moving average of 8 × 8 pixels (75% window overlap), the processing results in a field measurement of 96 × 60 velocity vectors with a temporal resolution of 15 velocity fields per second. With a typical field of view of 11 × 8 cm, the spatial resolution is 0.46 × 0.54 cm. In the present results, the maximum velocities are in the order of magnitude of 10 cm/s limiting the particle displacement to approximately 6 pixels. Since the location of the cross-correlation peak can be resolved with a sub-pixel accuracy of approximately 0.01 pixel (Willert and Gharib 1991), the maximum uncertainty based on the local velocity and vorticity magnitude is ±1% and ±3%, respectively.

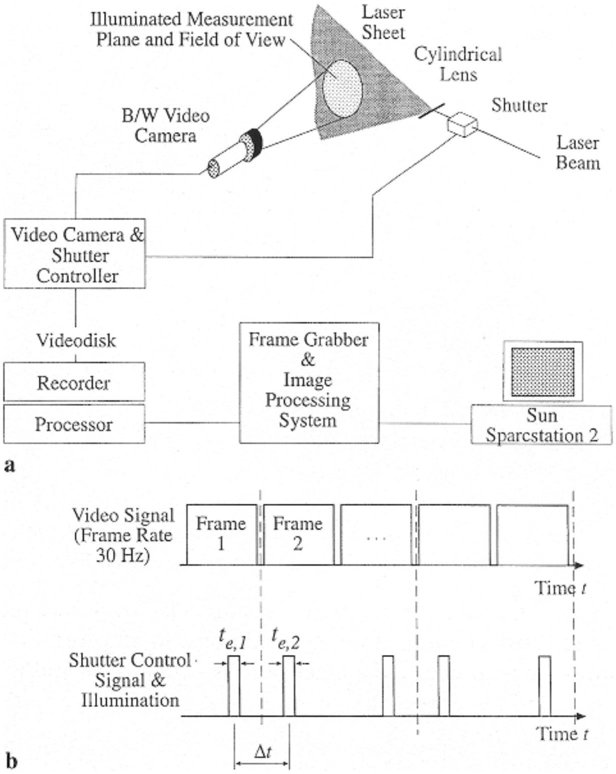

Fig. 2a, b. Digital Particle Image Velocimetry (DPIV). **a** Experimental setup and processing system, **b** Illumination control

3
Vortex-ring properties and circulation measurements

3.1
Overview and Initial conditions

Six different vortex rings were investigated in a Reynolds-number range of $830 \leqslant Re \leqslant 1650$. The Reynolds number is defined by the ratio of the circulation Γ to the kinematic viscosity ν, where the circulation $\Gamma = \Gamma_{2.5}$ was obtained from LDA measurements at a downstream position of $x^* = 2.5$. Throughout the remainder of this paper, the temporal origin $t = 0$ corresponds to the initiation of the piston motion, while length scales that are normalized by the nozzle diameter D_0 are marked by an asterisk (e.g., $x^* = x/D_0$).

Table 1. Specification of nominal piston motion

Reynolds number Re	830	950	1080	1150	1260	1650
Time [s]:						
• Accel., Decel.	0.10	0.10	0.10	0.10	0.10	0.10
• Constant velocity	0.25	0.21	0.18	0.15	0.10	0.05
• Total	0.45	0.41	0.38	0.35	0.30	0.25
Velocity [cm/s]:						
• Maximum velocity $U_{0,\max}$	5.8	6.6	7.4	8.1	10.2	13.5
• Average velocity $\bar{U}_0$	4.5	4.9	5.4	5.8	6.8	8.1
Acceleration/deceleration [cm/s^2]:						
• $\lvert a_{up}\rvert = \lvert a_{do}\rvert$ = constant	58.4	65.4	73.7	81.3	101.6	134.6

Table 1 specifies the trapezoidal piston-velocity profiles that were selected as nominal initial conditions. In all cases, the piston-stroke to nozzle-diameter ratio is $L_0/D_0 = 0.68$ and the acceleration and deceleration periods are $t_{up} = t_{do} = 0.1$ s. As the typical example in Fig. 3 shows, the measured piston motion is in good agreement with the nominal velocity profile.

In Fig. 4, the initial roll-up of a vortex-ring with a Reynolds number of $Re = 1080$ is shown. After the piston comes to rest, Figs. 4-III and 4-IV depict the formation of an opposite-sign secondary vortex ring (stop vortex) that propagates into the cylinder volume. Similar to the results of Didden (1979), Fig. 5 indicates that the visual trajectories of the primary spiral centers are spatially independent of the Reynolds number. The non-dimensional vortex-ring diameter D^* (defined by the distance between the spiral centers) initially increases to 1.05 and expands to a maximum value of 1.25 at $x^* \approx 0.16$. Subsequent to the expansion, the diameter decreases to its fully developed value of $D^* \approx 1$ ($D = 2.97 \pm 0.03$ cm) at $x^* \approx 0.6$. The location of the maximum at $x^* \approx 0.16$ indicates that the contraction of the diameter starts during the deceleration period of the piston, i.e., before the piston comes to rest at $x^* \approx 0.18$.

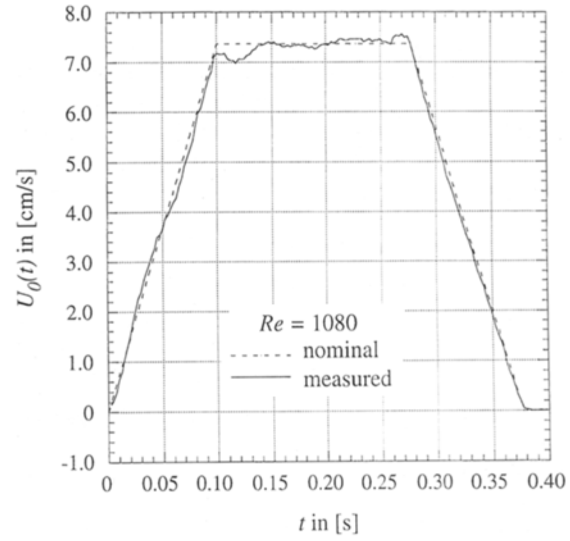

Fig. 3. Evolution of the nominal and measured piston-velocity profile for $Re = 1080$

3.2 Results

Velocity, vorticity and circulation

Similar to Glezer and Coles (1990) and as indicated in Fig. 1, a first estimate of the vortex-ring circulation was obtained by conducting single-point LDA measurements of the center-flow velocity at the downstream positions $x_M^* = 1$ and $x_M^* = 2.5$.[1]

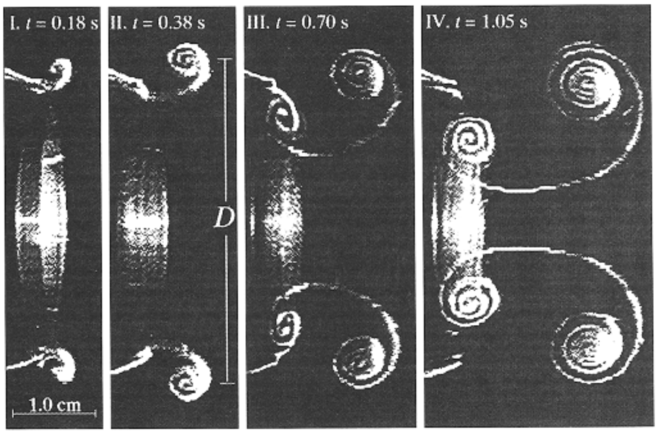

Fig. 4. Initial vortex-sheet roll-up of a vortex ring with $Re = 1080$

---

[1] The circulation of a vortex ring at the position x_M can be estimated by evaluating the closed-line integral of the velocity field along a rectangular control contour S that is located in the upper half-plane $y > 0$ and includes the center-line x. Since the velocity field of a vortex ring decays proportional to r^{-3} (Batchelor 1967), and the length of the contour increases only proportional to r, the closed-line integral, if evaluated at $r \rightarrow \infty$, reduces to an integral along the center line x.

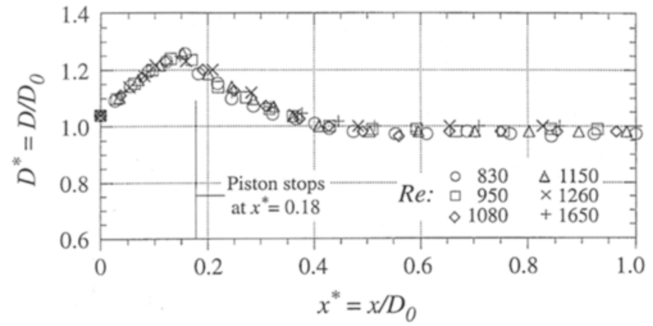

Fig. 5. Spatial evolution of the vortex-ring diameter

Assuming a constant propagation velocity of the vortex ring at the downstream position x_M (Taylor hypothesis), the integration of the velocity along the center line is transformed into an integration over time and yields

$$\Gamma_M = U_{V,M} \int_0^\infty u_M(t)\,\mathrm{d}t \tag{1}$$

Provided that the Taylor hypothesis applies, Eq. (1) gives the circulation Γ_M with the local propagation velocity $U_{V,M}$ and the center-flow velocity $u_M(t)$ measured at the position x_M.

The local propagation velocities of the vortex rings were obtained from visual trajectory and DPIV measurements. In all flow cases, the integration of velocity fluctuations averaged out to zero and resulted in a good initial and asymptotic behavior of the circulations Γ_1 and $\Gamma_{2.5}$. The asymptotic values of Γ_1 and $\Gamma_{2.5}$ are listed in Table 2, Sect. 3.3 for comparison with results of DPIV measurements.

The LDA-velocity and circulation measurements were complemented by comprehensive DPIV mapping of the velocity-vector fields in the plane $z=0$. As a typical example, Figs. 6a and b show a single realization of the measured velocity-vector field and the corresponding vorticity contours of a vortex ring with Reynolds number $Re=1150$. The azimuthal vorticity component $\omega = \partial v/\partial x - \partial u/\partial y$ was calculated by using a second order finite-difference scheme.

Figures 7a and 7b show spatial cross sections of the u- and v-velocity components extracted from the DPIV data of the six flow cases. In Fig. 7a, the velocity components along the axis $y^*=0$ (center-line) are shown. Due to the symmetry of the velocity field, the v-component is in all flow cases small compared to the u-component and in the range of ± 0.1 cm/s. For the flow cases $Re=830$ and $Re=1650$, Fig. 7a also shows the velocity profiles that result from the Taylor transformation of the LDA-data. The transformed LDA-velocity profiles agree well with the DPIV data over a relatively large section centered at $x^*=2.5$, i.e., the position where the propagation velocity of the vortex rings was measured. Regarding the Taylor hypothesis and the assumption of a constant propagation velocity, the effect of the decay of the propagation velocity is more apparent at lower Reynolds numbers (i.e., lower propagation velocities) which leads to the under- and overestimation of the transformed u-velocity components at $x^*<2.1$ and $x^*>2.9$, respectively.

Figure 7b shows the velocity components along the line that connects the core centers (i.e., the peak vorticities) of the

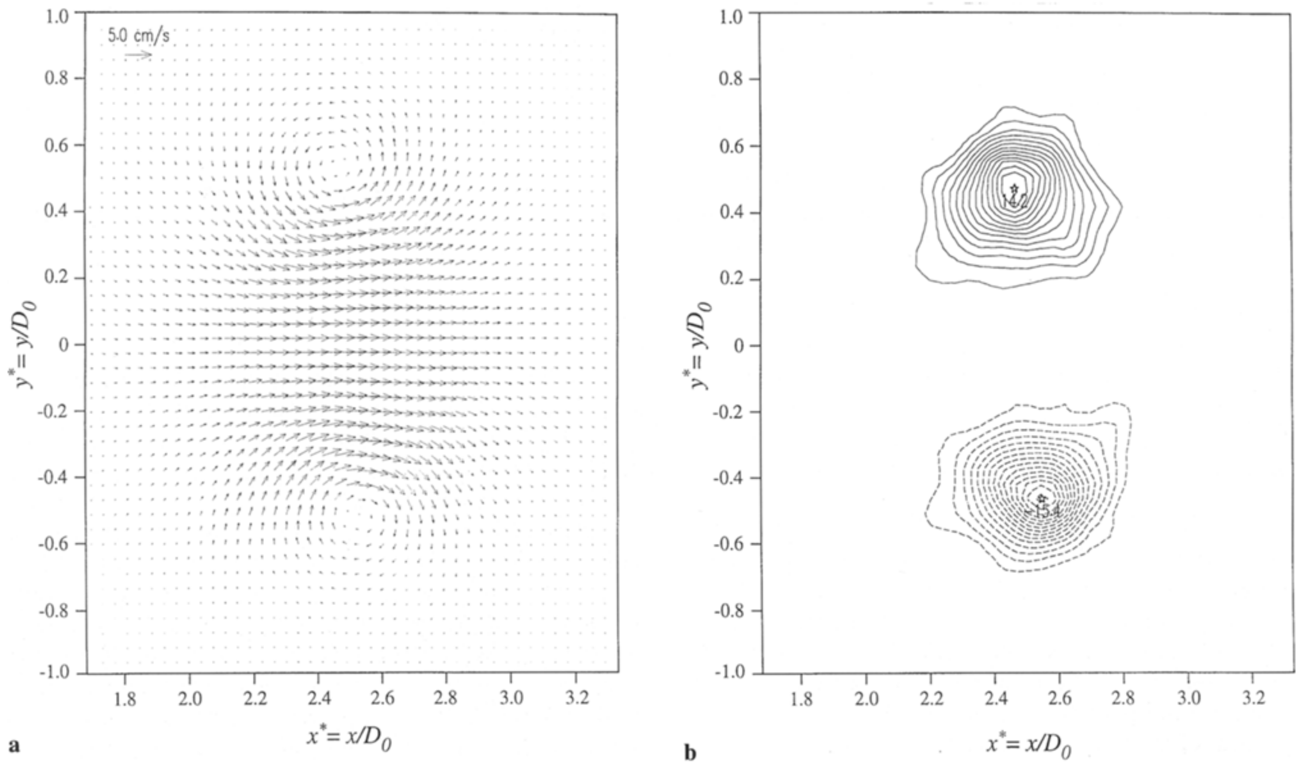

Fig. 6a, b. DPIV measurements of the flow field of a vortex ring in the plane $z=0$ with $Re=1150$ at $x^*=2.5$. **a** Velocity-vector field; **b** vorticity contours with peak vorticities indicated in the core centers, first contour: $\omega_1 = \pm 1.0\ \mathrm{s}^{-1}$ step size: $\Delta\omega = \pm 1.0\ \mathrm{s}^{-1}$

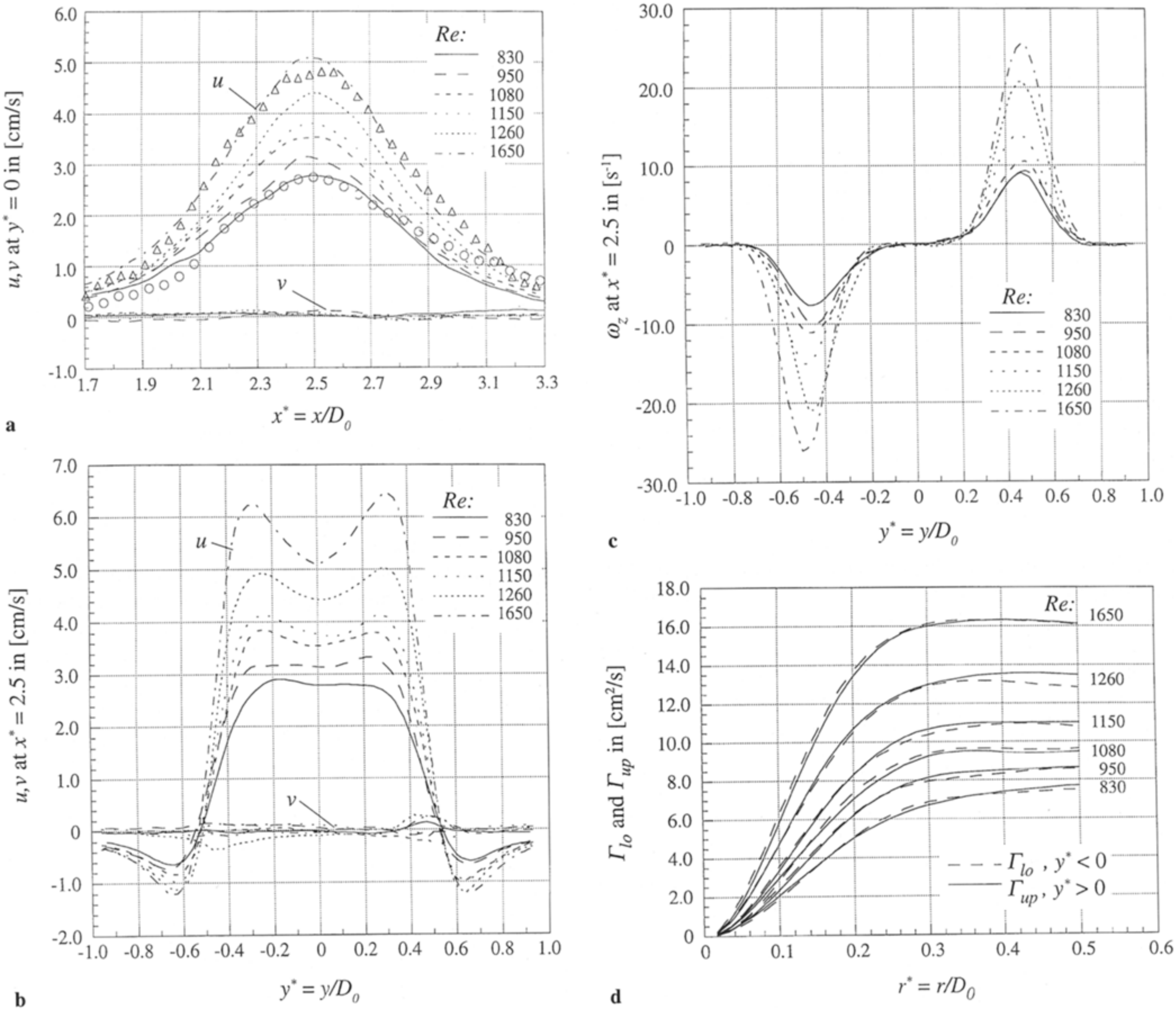

Fig. 7a–d. Vortex-ring properties obtained from DPIV measurements. **a** Velocity profiles at $y^* = 0$ and Taylor transformed LDA-velocity profiles (0, Δ); **b** velocity profiles at $x^* = 2.5$; **c** vorticity profiles at $x^* = 2.5$; **d** radial distribution of core circulation at $x^* = 2.5$

vortex rings at $x^* \approx 2.5$. Again, due to the symmetry of the velocity field, the resulting v-velocity components are small (± 0.3 cm/s). The u-velocity profiles of the higher Reynolds number cases are characterized by a typical U-shaped velocity distribution in the inner region of the vortex ring. In order to determine the circulation from the LDA data, the local propagation velocity of the vortex rings was estimated from the u-velocity profiles by forming the mean value of the velocity minimum and maximum (Galilean transformation).

In Fig. 7c, the vorticity distributions along the cross section $x^* \approx 2.5$ are shown. In good agreement with the vortex-ring diameters measured by means of flow visualization, the distance between the vorticity peaks is 2.8 ± 0.1 cm and independent of the Reynolds number. The magnitudes of the peak vorticities of the upper ($y > 0$) and lower core ($y < 0$) agree well and deviate less than $\pm 5\%$ from their corresponding mean value.

Figure 7d shows the distribution of the upper- and lower-core circulations, where the local circulation was calculated along a closed circular path of radius r centered at the location of the peak vorticity. In each flow case, the radial development of the upper and lower circulations agrees well with a maximum deviation of 5%.

In addition to the circular path integration, the circulations were also determined on a rectangular control contour. The coordinates of the diagonal corners of the control contour were chosen to be $(x_1^*, y_1^*) = (1,0)$ and $(x_3^*, y_3^*) = (4, \pm 1.25)$. The resulting magnitudes of the upper- and lower-core circulations are in good agreement and deviate less than 3% from each other. This agreement is also indicated by a small residual circulation $\Delta\Gamma$ that is evaluated for the entire flow field on a rectangular contour with diagonal corners $(x_1^*, y_1^*) = (1, -1.25)$ and $(x_3^*, y_3^*) = (4, +1.25)$. In all flow cases, $\Delta\Gamma$ does not exceed more than 3% of the corresponding magnitude of the vortex-ring circulation. The mean asymptotic circulations resulting from the circular path integration, and the circulations that were evaluated on a rectangular control contour are listed in Table 2, Sect. 3.3.

Estimate of the core size

From the DPIV data presented in Fig. 7, the core size of the vortex rings can be estimated in several different ways. In Fig. 7b, the distance between the minima and maxima of the u-velocity profiles indicates core diameters between $0.35 \leqslant \sigma^* \leqslant 0.45$. However, the vorticity profiles and the radial distribution of circulations presented in Figs. 7c and d indicate both larger core diameters in the range of $0.6 \leqslant x^* \leqslant 0.8$. A comparison of the velocity and vorticity profiles shows that the vorticity is non-zero at locations where the gradient $\partial u/\partial y = 0$. This suggests that the term $\partial v/\partial x$ contributes to the magnitude of the vorticity, and that the extracted u-velocity profiles do not exactly satisfy the symmetry condition $\partial v/\partial x = 0$.

Since the velocity and vorticity profiles are determined along a certain spatial cross section, any variation of the core diameter over the core region is neglected. Therefore, in terms of the assumption of a circular core region, the integral measure resulting from the radial asymptotic behavior of the circulation is regarded here as the more accurate estimate for an average core diameter. The results are listed in Table 2, Sect. 3.3 and indicate a reduction of the core size with increasing Reynolds number (from $\sigma^* = 0.8$, $Re = 830$ to $\sigma^* = 0.6$, $Re = 1650$).

Vorticity distribution in the core region

Figure 8 shows a scatter diagram of the vorticity data that were extracted along the cross section $x^* \approx 2.5$. The y-coordinate and the vorticity distribution of the six flow cases (upper and lower cores) are normalized by the corresponding core radii a and peak vorticities ω_0:

$$\bar{y} = y/a, \quad a = 0.5\sigma^* D_0 \quad \text{and} \quad \bar{\omega} = \omega/\omega_0, \quad \omega_0 = \omega(y_0^*), \tag{2a}$$

where $\omega_0 > 0$ for $y_0^* > 0$ and vice versa. The inner ($y^* < |y_0^*|$) and outer core regions ($y^* > |y_0^*|$) of the vortex rings are mapped to the half planes $\bar{y}_1 > 0$ and $\bar{y}_1 < 0$ by using a transformation with the normalized vorticity peaks $\bar{\omega}_0 = 1$ centered at $\bar{y}_1 = 0$:

$$y^* > 0\colon \; \bar{y}_1 = \bar{y} - \bar{y}_0 \quad \text{and} \quad y^* < 0\colon \; \bar{y}_1 = \bar{y}_0 - \bar{y} \tag{2b}$$

As is evident in Fig. 8, the vorticity distributions are nearly symmetric about $\bar{y}_1 = 0$. In the inner regions of the vortex rings at $\bar{y}_1 < -0.6$, vorticity diffusion between the opposite-sign vortices leads to a small asymmetric broadening of the vorticity distribution; due to their relatively large core size, this effect is predominantly visible in the lower Reynolds number flow cases. The majority of the data collapses onto a self-similar distribution that is well approximated by a Gaussian vorticity profile of a Lamb–Oseen vortex (e.g., Saffman 1992). The Lamb–Oseen vortex is an exact solution of the two-dimensional Navier–Stokes equations (diffusion equation) and yields a vorticity distribution of

$$\omega = \frac{\Gamma_0}{4\pi\nu t} \exp\left(-\frac{r^2}{4\nu t}\right) \tag{3a}$$

where Γ_0 is the initial circulation, t the time, ν the kinematic viscosity, and r the radial coordinate of the core region. Using Eqs. (2) to normalize Eq. (3a) and applying the boundary condition $\bar{\omega} = 1$ at $\bar{y}_1 = 0$ gives

$$\bar{\omega} = \exp\left(-\eta^2 \bar{y}_1^2\right) \quad \text{with } \eta^2 = \left(\frac{a}{a_0}\right)^2 = \frac{\pi a^2 \omega_0}{\Gamma_0} \tag{3b}$$

Since the initial condition of the Lamb–Oseen vortex is defined by a Dirac δ-function of the circulation Γ_0 at time $t = 0$, it is experimentally difficult, if not impossible, to determine the accurate temporal origin. As Eq. (3b) indicates, the applied normalization has the advantage that it eliminates the explicit variable time t or, more accurately, the product νt. Therefore, the Gaussian vorticity distribution is fully determined by the time dependent factor η that represents the ratio of the actual core radius a to the core radius a_0. The latter is defined by $a_0^2 = 4\nu t = \Gamma_0/(\pi\omega_0)$ and designated as "equivalent core radius".[2]

The exponential factors of the Gaussian vorticity distributions defined by $\eta^2 = \pi a^2 \omega_0/\Gamma_0$ result from the DPIV data at the cross section $x^* = 2.5$ and are listed in Table 2, Sect. 3.3. Using the circulations evaluated on a rectangular control contour yields a mean value of $\eta^2 = 4.7 \pm 0.7$. As Fig. 8 indicates, the minimum and maximum values of η^2 lead to a good agreement with the measured vorticity profiles. The cut-off behavior at $|\bar{y}_1| = 1$ can be determined by the ratio of the circulations $\Pi = \Gamma_a/\Gamma_\infty$, where Γ_a and Γ_∞ are evaluated within the boundaries $|\bar{y}_1| \leqslant 1$ and $|\bar{y}_1| \to \infty$, respectively. In the case of a Gaussian profile, the cut-off ratio is given by $\Pi = 1 - \exp(-\eta^2)$ with a value of $\Pi = 0.99$ for $\eta^2 \approx 4.6$. Therefore, the experimental mean value of $\eta^2 = 4.7$ leads to an approximation in terms of the circulation Γ_∞ of better than 99%.

The data in Fig. 8 are also compared to other analytical expressions of vorticity distributions such as $\bar{\omega} = (\bar{y}_1^2 - 1)^2$; $|\bar{y}_1| \leqslant 1$ (Widnall et al. 1974) and $\bar{\omega} = \operatorname{sech}^2 \bar{y}_1$ (Maxworthy 1977). In contrast to the Lamb–Oseen vortex, the latter two expressions lead to relatively wide-spread distributions that overestimate the circulation of the vortex ring (e.g., the integration of the distribution $\bar{\omega} = \operatorname{sech}^2 \bar{y}_1$ in the interval $|\bar{y}_1| \leqslant 1$ results in $\Gamma_a = 0.656\pi a^2 \omega_0$ and yields errors of up to 300%). Additionally, the integration of the sech^2-distribution in the interval $|\bar{y}_1| \to \infty$ results in $\Gamma_\infty = 2 \ln 2\pi a^2 \omega_0$ and, as Fig. 8 indicates, leads to a poor cut-off ratio of $\Pi = 0.47$.[3]

---

[2] The definition of a_0 characterizes a Rankine vortex with uniform distribution of the maximum vorticity of a Lamb–Oseen vortex in the core region, i.e. $\omega = \omega_0 = \text{const.}$ for $r \leqslant a_0$ and $\omega = 0$ for $r > a_0$. The circulation of this vortex is equal to the initial circulation $\Gamma_0 = \pi a_0^2 \omega_0$. Therefore, the factor $\eta^2 = \pi a^2 \omega_0/\Gamma_0$ in Eq. (3b) can be regarded as a measure for the slenderness of the Gaussian vorticity profile.

[3] It is not clear from Maxworthy (1977) which length scale was used to normalize his radial coordinate r_1 in the sech^2-distribution. In order to be consistent with the present results, we used the core radius a for the normalization. Note: As one referee suggested, a sech$^2(3\bar{y}_1)$-distribution leads to a good agreement with the data; however, the additional factor would imply three times smaller core radii which is not consistent with the results of the present measurements.

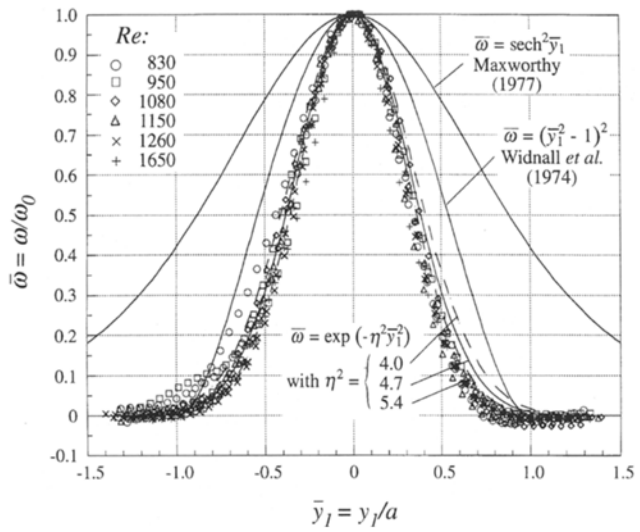

Fig. 8. Normalized vorticity data in comparison to analytical vorticity distributions proposed by Widnall et al. (1974) and Maxworthy (1977)

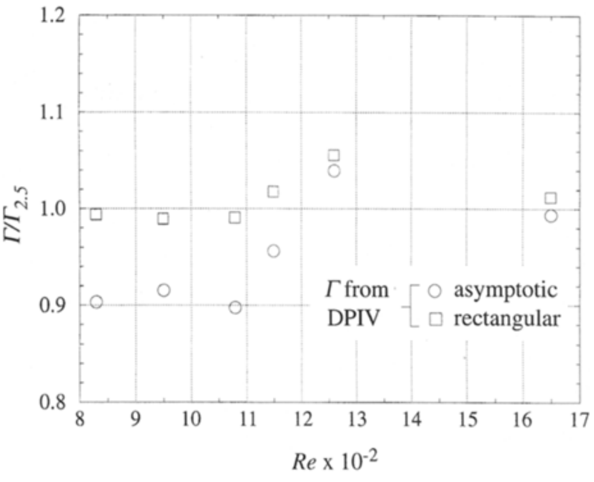

Fig. 9. Comparison of the circulations obtained from DPIV and LDA measurements at $x^* = 2.5$

3.3
Discussion of the circulation measurements

The results of the circulation measurements are summarized in Table 2 and Fig. 9. A first estimate of the initial vortex-ring circulation Γ_0 can be obtained from the piston-motion profiles by integrating the vorticity flux across the nozzle-exit plane (vorticity-flux or slug-flow model). The derivation of the model for trapezoidal piston-velocity profiles is given in the Appendix, and the resulting circulations are listed in Table 2.

Similar to the results of Didden (1979) and Glezer and Coles (1990), a comparison of the circulations obtained from the vorticity-flux model (Γ_0) and LDA measurements (Γ_1) shows that the vorticity-flux model underestimates the initial circulations by up to 60%. The major reason for this disagreement is due to the boundary-layer approximation in the model that assumes $\partial p/\partial r = 0$; therefore, the model neglects the balance between radial negative pressure gradients and centrifugal forces during the roll-up of the vortex sheet. Consequently, the outer edge velocity of the boundary layer is substantially larger than the piston velocity which causes the model to underestimate the vorticity flux and the circulation. In the case of short stroke piston motions (here: $L_0/D_0 = 0.68$), this effect strongly dominates other effects that are not accounted for by the model (e.g., entrainment of opposite sign vorticity from the boundary layer at the outer edge of the nozzle and blockage effects due to the boundary layer growth in the nozzle).

Table 2. Properties of the investigated vortex rings with $[\Gamma] = [\mathrm{cm}^2/\mathrm{s}]$. The wave numbers n_1, n_2, and n_3 of the bending instabilities result from the present experiments, the theory of Widnall et al. (1974), and the second instability mode of Saffman (1978), respectively

Reynolds number Re	830	950	1080	1150	1260	1650
Vorticity-flux model:						
• Velocity-Program Factor P	1.16	1.18	1.20	1.21	1.25	1.30
• Circulation Γ_0	5.3	5.9	6.6	7.2	8.6	10.7
• Circulation $\Gamma_{0,c}$ from Eq. (4a)	8.6	9.6	10.6	11.5	13.9	17.2
• Circulation $\Gamma_{0,c}$ from Eq. (4c)	8.7	9.6	10.7	11.6	13.5	16.4
LDA:						
• Circulation Γ_1	9.0	10.1	11.0	11.9	12.9	17.0
• Circulation $\Gamma_{2.5}$	8.3	9.5	10.8	11.5	12.6	16.5
DPIV:						
• Circulation $\Gamma_{2.5}$ (circular)	7.5	8.7	9.7	11.0	13.1	16.4
• Circulation $\Gamma_{2.5}$ (rectangular)	8.3	9.4	10.7	11.7	13.3	16.7
• Core diameter σ [cm]	2.4	2.4	2.3	2.2	2.1	1.8
• Factor η^2 of Gaussian distrib.	4.6	4.6	4.2	4.7	5.4	4.0
Bending instabilities:						
• Onset at x [cm], t [s]	–	–	–	40, 32	38, 22	34, 14
• Wave number n	–	–	–	5, 5, 4	6, 5, 6	7, 6, 7

Didden (1979) and Pullin (1979)[4] provide correction formulas for the circulation Γ_0. Based on the vorticity-flux model and LDA measurements, Didden gives an empirical correction with

$$\frac{\Gamma_{0,c}}{\Gamma_0}=1.14+0.32\left(\frac{L_0}{D_0}\right)^{-1}, \quad \left(\frac{L_0}{D_0}\right)>0.6 \text{ and } Re=\frac{\Gamma_0}{\nu}<7000 \tag{4a}$$

where $\Gamma_{0,c}$ is the corrected circulation. In the present flow cases with constant piston-stroke to nozzle-diameter ratios ($L_0/D_0=0.68$), Eq. (4a) yields $\Gamma_{0,c}=C\Gamma_0$ with a correction factor of $C=1.61$. As Table 2 indicates, the results of Didden's empirical formula lead to a good agreement with the circulations Γ_1 obtained from LDA measurements (the maximum deviation between $\Gamma_{0,c}$ and Γ_1 is less than 8%).

Pullin's correction is based on the self-similar roll-up of a two-dimensional vortex sheet and yields for a tube geometry with impulsive piston motion

$$\frac{\Gamma_{0,c}}{\Gamma_0}=1.41\left(\frac{L_0}{D_0}\right)^{-2/3} \quad \text{with} \left(\frac{L_0}{D_0}\right)\ll 4.7 \tag{4b}$$

In a first order approximation, using the actual stroke to nozzle-diameter ratio of the trapezoidal piston motion ($L_0/D_0=0.68$), Eq. (4b) yields a factor of $C=1.82$. The latter is 13% larger than the result of Didden's correction formula and overestimates the corrected circulations with respect to Γ_1 by up to 20%.

However, the result of Pullin's correction formula can be improved by defining an equivalent stroke to nozzle-diameter ratio that corresponds to an impulsive piston displacement with average velocity $\bar{U}_0$ and generates the same amount of circulation as the trapezoidal velocity profile. According to the vorticity-flux model and the definition of the velocity-program factor P (Appendix, Eq. (A.5)), the equivalent piston-stroke to nozzle-diameter ratio results to $L_e/D_0=P(L_0/D_0)$. Replacing L_0/D_0 with L_e/D_0 in Eq. (4b), Pullin's correction formula for a tube geometry with equivalent impulsive piston motion yields

$$\frac{\Gamma_{0,c}}{\Gamma_0}=1.41\left(P\frac{L_0}{D_0}\right)^{-2/3} \quad \text{with} \left(P\frac{L_0}{D_0}\right)\ll 4.7 \tag{4c}$$

The program factors P of the trapezoidal velocity profiles are listed in Table 2. Equation (4c) gives correction factors in a range of $1.53\leqslant C\leqslant 1.64$ that increase with decreasing Reynolds number, i.e., with decreasing trapezoidal shape of the piston-velocity profile. This result leads to a good agreement with Didden's correction ($C=1.61$) and a deviation of less than 4% from the measured circulations Γ_1 (see Table 2).

Figure 9 shows a comparison of the circulations obtained from LDA and DPIV measurements at the downstream position $x^*=2.5$. The resulting circulations from the DPIV data are normalized by the corresponding results of the LDA measurements. Using a rectangular control contour leads to a good agreement with the results of the LDA measurements over the entire Reynolds-number range. Between $830\leqslant Re\leqslant 1080$, the asymptotic values of the circulations that were evaluated on a circular control contour are consistently 10% smaller than the circulations obtained from the LDA measurements, while for $Re\geqslant 1150$, good agreement is achieved with a maximum deviation of 5% at $Re=1260$. A possible reason for the consistent disagreement in the lower Reynolds number flow cases might be due to the non-concentrated vorticity distributions, where, with increasing radius, the circular control contour partially penetrates into the opposite-sign vorticity region.

4
Vortex-ring trajectory measurements

In this section, results of visual measurements of vortex-ring trajectories are presented and compared to various analytical models. The trajectories were measured by using a calibrated video system with a field of view that covers a dowstream distance of 30 cm from the nozzle-exit plane (i.e., approximately 10 ring diameters). The video images were digitized with a resolution of 768 × 480 pixels which results in a spatial wavelength resolution of 0.08 cm in the downstream direction. The trajectory data are based on 10 independent realizations per flow case and were found to be repeatable within ±4% of the presented mean values.

Based on the analytical solution of Thomson (in Helmholtz 1867) and Hicks (1885) (see, e.g., Lamb 1932), Tung and Ting (1967) and Saffman (1970) derived an analytical model for the unsteady, viscous motion of vortex rings that yields the following relation for the evolution of the propagation velocity:

$$U_V(\tau)=\frac{\Gamma}{2\pi D}\left\{\log\left(\frac{4}{\tau}\right)-0.558+O[\tau\log\tau]\right\}$$

$$\text{with } \tau=\frac{\sqrt{4\nu t}}{D} \tag{5}$$

where D designates the diameter, Γ the circulation, t the time and ν the kinematic viscosity. The major assumptions in that model are that the relative core size is small and that the vortex-ring diameter is constant. The latter follows from Saffman, who shows that the vorticity distribution in the core region asymptotes a Gaussian profile. Therefore, the rate of change of the circulation is negligible for viscous time scales $\tau^2\ll 1$ which, in combination with the condition of a constant impulse ($I\propto\Gamma D^2$), results in a constant vortex-ring diameter. Using the normalized variables $U_V^*=2\pi U_V D/\Gamma$ for the propagation velocity and $t^*=\nu t/(4D^2)$ for time, Eq. (5) yields

$$U_V^*(t^*)=-\frac{1}{2}\log t^*-0.558+O[\tau\log\tau] \tag{6}$$

Figure 10a shows a comparison of the experimental data with Saffman's normalized relation (Eq. (6)). The diameter D_0 and the circulation Γ_1 are used for the normalization of the data, where Γ_1 was obtained from LDA measurements at the downstream position $x^*=1$.

In the range $4\cdot 10^{-4}\leqslant t^*\leqslant 2\cdot 10^{-3}$ ($1.4\,\text{s}\leqslant t\leqslant 7.2\,\text{s}$), the evolution of the vortex-ring propagation velocities is well approximated by the theory. During the formation process between $0\leqslant t^*<4\cdot 10^{-4}$ ($0\,\text{s}<t<1.4\,\text{s}$), the theoretical assumption of a constant ring diameter is clearly not satisfied.

---

[4] In Pullin (1979), Eq. (9) has been misprinted. The exponent should read +2/3 instead of −2/3.

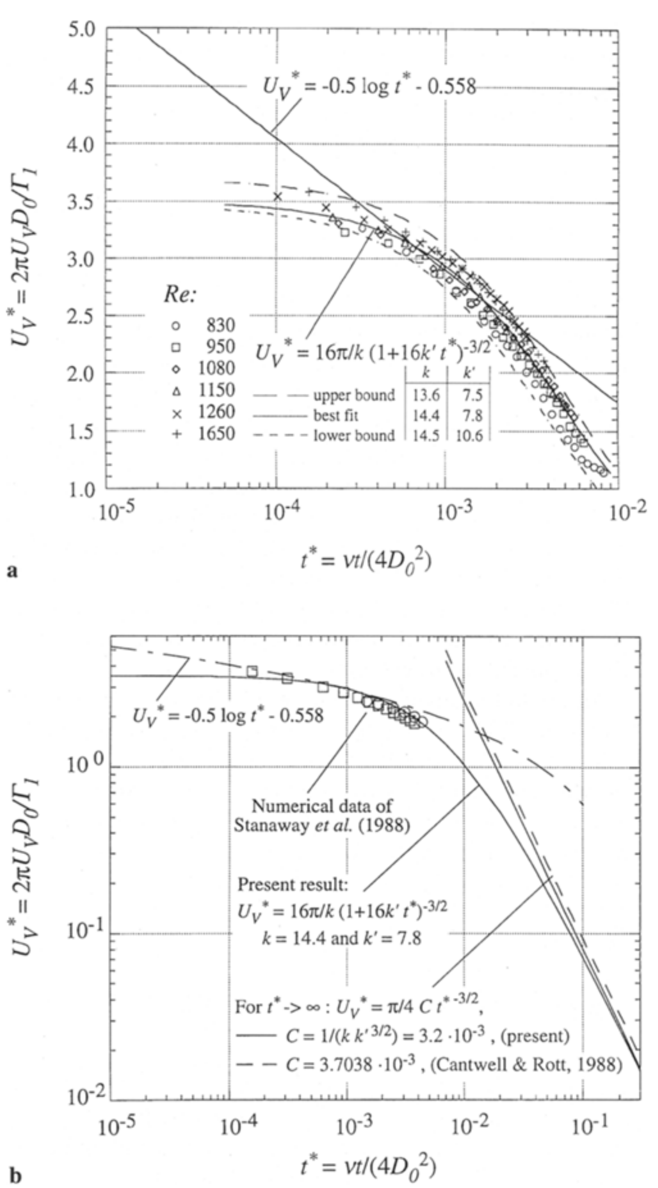

Fig. 10a, b. Evolution of the propagation velocity. **a** Comparison with analytical models of Saffman (1970); **b** comparison with numerical data of Stanaway et al. (1988) and the exact solution of Cantwell and Rott (1988) in the asymptotic case $t \to \infty$

The non-concentrated spiral distribution of vorticity in the core region as well as the initial expansion of the vortex-ring diameter tend to decrease the initial propagation velocity, while the subsequent diameter contraction (see Fig. 5) causes an acceleration of the vortex ring. For $t^* > 2 \cdot 10^{-3}$ ($t > 7.2$ s), one can conjecture that viscous diffusion leads to an increase of the core size beyond the measured values of $0.6 \leqslant \sigma^* \leqslant 0.8$ and causes vorticity cancellation between the core regions of opposite-sign vorticity. This process might lead to a "non-negligible" decrease of the circulation and, consequently, to a faster decay of the propagation velocity.

In addition to Eq. (5), Saffman (1970) provides a second relation for the evolution of the propagation velocity which does not include the assumption of small core sizes and allows the viscous length scale to be in the order of magnitude of the diameter of the vortex ring, i.e., $\tau^2 \sim 1$. Saffman's analysis is based on dimensional arguments and is briefly repeated here.

The propagation velocity U_V can be assumed to be proportional to the specific impulse $I_s = I/\rho$ divided by the fluid volume $V \propto R^3$ of the vortex ring, i.e.,

$$U_V = \frac{I_s}{kR^3} \tag{7}$$

where k designates the proportionality constant of the impulse. The viscous decay of the circulation can be formulated as

$$\frac{\mathrm{d}}{\mathrm{d}t}(U_V R) = -k' \frac{\nu U_V}{R} \tag{8}$$

using the relation $\Gamma \propto U_V R$ and a second proportionality constant k' for the viscous decay. Since the impulse $I \propto \Gamma R^2$ is invariant, Eq. (8) can be integrated by using Eq. (7) yielding

$$R^2 = R_0^2 + k'\nu t \quad \text{and} \quad U_V = \frac{I_s}{k}(R_0^2 + k'\nu t)^{-3/2} \tag{9a, b}$$

In contrast to Eq. (5), where the diameter of the vortex ring was assumed to be constant, Eq. (9a) describes the growth of the vortex ring with initial radius R_0 due to viscous decay. Using the impulse $I_s = \Gamma_0 D_0^2$ and the normalization procedure applied to Eq. (6), the non-dimensional form of Eqs. (9a, b) yields

$$D^{*2} = (1 + 16k't^*), \quad \text{and} \quad U_V^* = \frac{16\pi}{k}(1 + 16k't^*)^{-3/2} \tag{10a, b}$$

Figure 10a shows Eq. (10b) fitted to the velocity data by adjusting the two independent constants k and k'. The data is bound by the constants $k = 13.6$ and $k' = 7.5$ (upper bound) and $k = 14.5$ and $k' = 10.6$ (lower bound). The best fit, achieved with $k = 14.4$ and $k' = 7.8$, results in an excellent agreement of Eq. (10b) over the entire range of the experimental data.

The resulting range of the proportionality constant of the impulse ($13.6 \leqslant k \leqslant 14.5$) is within the valid range bounded by a potential (lower bound) and a spherical Hill's vortex ring (upper bound). The specific impulse of a potential vortex ring with small core size and constant vorticity distribution in the core region (Rankine vortex) is $I_P = \pi/4 \Gamma D_0^2$. Its propagation velocity can only be evaluated assuming a small, finite core size $\sigma^* \ll 1$ yielding $U_{V,P} = \Gamma/(2\pi D)\log(1/\sigma^*)$. The proportionality constant of the impulse results to $k_P = 4\pi^2/\log(1/\sigma^*)$, and the limit $\sigma^* \to 0$ gives the lower bound of k with $k_P \to 0$. The specific impulse of a spherical Hill's vortex ring is $I_H = \pi/4 D_H^3 U_{V,H}$, where D_H designates the diameter of the sphere. Considering that the diameter of a spherical vortex ring is $D = 1/2\, D_H$, the upper bound for k results in $k_H = 16\pi \approx 50.3$.

A comparison of the experimental values of k with the range of $0 < k \leqslant 50.3$ suggests that the investigated vortex rings are more similar to a potential ring with small core size than to a spherical Hill's vortex ring. This agrees well with the observation that the cross-sectional shape of the vortex rings is not circular, but elliptical. The core diameter of an "equivalent potential vortex ring" can be evaluated by using the relation $k = k_P = 4\pi^2/\log(1/\sigma^*)$ yielding $\sigma^* \approx 0.1$. The latter might be an indication for the partially good approximation that results from Saffman's relation for vortex rings of small core sizes (Eq. (6)). However, the resulting potential core diameter does not agree with the equivalent core diameters $\sigma_0^* = 2a_0/D_0 \approx 0.3$ that are obtained from the Gaussian vorticity distributions in Sect. 3.2 and also represent a Rankine vortex.

The range of the proportionality constant for the viscous decay ($7.5 \leqslant k' \leqslant 10.6$) indicates a relatively small temporal increase of the vortex-ring diameter. For example, using $k' = 7.8$ from the best data fit, Eq. (10a) yields a diameter increase of $D^* = 1.06$ at $t^* = 10^{-3}$ ($t = 3.6$ s) and $D^* = 1.5$ at $t^* = 10^{-2}$ ($t = 36.0$ s). These results are in good agreement with the observation that the growth of the vortex rings is relatively weak.

Figure 10b shows a log–log plot of the experimental data (represented by Eq. (10b) with $k = 14.4$ and $k' = 7.8$) in comparison to numerical results of Stanaway et al. (1988) and the exact asymptotic solution of Cantwell and Rott (1988) for $t \to \infty$.

As part of their numerical study, Stanaway et al. investigated the behavior of vortex rings in the asymptotic limit $t \to 0$ using Gaussian vorticity distributions with small Reynolds numbers ($Re \to 0$) and small core diameters ($\sigma^* \to 0$) as initial conditions. In comparison to Saffman's relation for small core sizes (Eq. (6)) which can be assumed to be well-suited for the preceding initial conditions, the numerical results suggest a slightly faster decay of the propagation velocity and a relaxed error estimate of $O(\tau^2 \log \tau)$ instead of $O(\tau \log \tau)$. As is evident in Fig. 10b, the computed propagation velocities (initial conditions $Re = 200$, $\sigma^* = 0.35$ and $Re = 800$, $\sigma^* = 0.12$) are initially in good agreement with Eq. (6). However, for $t^* > 2 \cdot 10^{-3}$ ($t > 7.2$ s), they are in better agreement with the present experimental results.

In the asymptotic limit $t \to \infty$, Philips (1956) derived a solution of the Stokes equation that is valid for the final decay of any vorticity distribution in an unbounded fluid being at rest at infinity. This solution has been verified by Kambe and Oshima (1975), who experimentally observed the final decay of the propagation velocity of vortex rings to be $U_V \propto t^{-3/2}$. In their numerical study, Stanaway et al. (1988) used a Stokes dipole in combination with a variety of initial conditions in order to determine the proportionality constant of the asymptotic decay. The constant was found to be in excellent agreement with the exact analytical solution of Cantwell and Rott (1988) who give the following relation for the asymptotic velocity of vortex rings:

$$U_V = C \frac{I}{\rho} (\nu t)^{-3/2} \quad \text{with } C = \frac{7}{240 \pi^{3/2} 2^{1/2}} = 3.7038 \cdot 10^{-3} \qquad (11)$$

As Eq. (11) indicates, the evolution of the drift velocity of the Stokes dipole depends only on the initial specific impulse $I_s = I/\rho$ and the kinematic viscosity. In the asymptotic limit $t \to \infty$, Saffman's relation for large core sizes (Eq. (10b)) yields Eq. (11) with the constant C defined by the proportionality constants k and k':

$$C = \frac{1}{k k'^{3/2}} \qquad (12)$$

The lower bound of the experimental data ($k = 14.5$, $k' = 10.6$) results in $C = 2.0 \cdot 10^{-3}$, while the upper bound ($k = 13.6$, $k' = 7.5$) gives $C = 3.6 \cdot 10^{-3}$. The results show that the investigated vortex rings decay like a Stokes dipole where the constant $C = 3.6 \cdot 10^{-3}$ resulting from the upper bound is in good agreement with the theoretical value of $C \approx 3.7 \cdot 10^{-3}$.

However, the majority of the data represented by the best fit values $k = 14.4$ and $k' = 7.8$ suggests a smaller experimental constant for the asymptotic decay resulting in $C = 3.2 \cdot 10^{-3}$. Therefore, one can conjecture that the vortex rings might reach their asymptotic limit earlier than predicted by the exact solution.

A possible reason for this difference in the proportionality constant might be the choice of the origin $t = 0$ that is defined in the experiments as the start of the piston motion. From the Gaussian vorticity distribution, a virtual origin of time can be estimated that corresponds to the theoretical initial condition of a Lamb–Oseen vortex (Dirac δ-function of the circulation at time $t' = 0$). The time difference between the virtual and experimental origin is defined by the equivalent core radius of Eq. (3b) and results in $\Delta t = t' - t = a^2/(4\eta^2 \nu) - t$. Using the experimental data at the downstream position $x^* = 2.5$ yields a temporal shift of $\Delta t^* \sim 10^{-4}$ ($\Delta t = 1.5 \pm 0.5$ s). However, it is evident from Fig. 10b that the time difference at large times, e.g., $t^* \sim 10^{-1}$ ($t \sim 10^2$ s) is $\Delta t^* \sim 10^{-2}$. Therefore, the difference between the virtual and experimental origin is much too small to account for the resulting time difference in the asymptotic limit.

One can conjecture that the smaller experimental constant of the majority of the data might be a result of non-linear and Reynolds-number dependent effects during the evolution of the vortex rings. For example, even a mild loss of vorticity into the wake of the vortex ring accumulates over large times and results in a faster reduction of the circulation and a decaying impulse of the vortex ring; therefore, the onset of the asymptotic stage characterized by the Stokes dipole solution might be reached earlier. In this regard, the formation of a wake can be caused by weak bending instabilities that were observed to form during the late evolution of the higher Reynolds number flow cases. The wave numbers of the instabilities are listed in Table 2 and were found to be in reasonable agreement with the theoretical results of Widnall et al. (1974) and the second-mode instability of Saffman (1978).

5

Conclusions

During the formation process of the laminar vortex rings, the roll-up geometry was observed to be independent of the Reynolds number within the investigated range of $830 \leqslant Re \leqslant 1650$. Regarding the initial conditions of the vortex rings, the application of the corrected vorticity-flux (slug-flow) model using Didden's (1979) empirical formula and a modified version of Pullin's (1979) model leads to a good agreement with circulations obtained from LDA-measurements at a downstream position of $x^* = 1$.

The results of the LDA and DPIV measurements at $x^* = 2.5$ show good agreement in terms of local velocities and vortex-ring circulations. The DPIV data of the six flow cases reveal that the vorticity distribution in the core region is self-similar and well-approximated by a Gaussian vorticity profile. An estimate of the core size is obtained from the radial asymptotic behavior of the circulation in the core region. The results indicate that the spatially averaged core diameters decrease weakly with increasing Reynolds number and are in a range of $0.6 \leqslant \sigma^* \leqslant 0.8$.

The visual trajectories of the vortex rings are in excellent agreement with analytical models of Saffman (1970), numerical calculations of Stanaway et al. (1988), and the exact analytical solution of Cantwell and Rott (1988) for the asymptotic drift velocity at $t \rightarrow \infty$. Assuming small core sizes and constant ring diameters, Saffman's model on the propagation velocity of vortex rings was found to deviate from the experimental data during the initial formation period and at relatively large times. However, a second model of Saffman which is based on dimensional arguments does not include the assumption of small core sizes and leads to an excellent agreement with the experimental data. The temporal evolution of the propagation speed is described by $U_V^* = 16\pi/k\ (1 + 16k't^*)^{-3/2}$, with the experimental constants $k = 14.4$ and $k' = 7.8$ obtained from the best data fit. In the asymptotic limit $t \rightarrow \infty$, the extrapolation of the data predicts that the velocity of the vortex rings approaches the drift velocity of a Stokes dipole. The exact solution of Cantwell and Rott (1988) yields an asymptotic drift velocity of $U_V^* = \pi/4C\ t^{*\,-3/2}$ with the proportionality constant $C = 3.7038 \cdot 10^{-3}$, while the present experimental data result in a smaller constant with $C = 1/(kk'^{3/2}) = 3.2 \cdot 10^{-3}$.

Appendix: The vorticity-flux (slug-flow) model

The vorticity-flux model is based on the assumption, that the change of the circulation Γ_0 in the upper half plane $y > 0$, $z = 0$ is equal to the vorticity flux across the nozzle-exit plane at $x = 0$:

$$\frac{\mathrm{d}\Gamma_0}{\mathrm{d}t} = \frac{\mathrm{d}}{\mathrm{d}t} \int_A \omega\, \mathrm{d}A = \int_\delta u \cdot \omega\, \mathrm{d}y = -\int_\delta u \frac{\partial u}{\partial y}\, \mathrm{d}y = \frac{1}{2} u_e^2 \tag{A.1}$$

where ω designates the azimuthal vorticity component, u the velocity component in the x-direction, $\mathrm{d}A = \mathrm{d}x \cdot \mathrm{d}y$ the area element, δ the boundary-layer thickness, and u_e the outer-edge velocity of the boundary layer.

Assuming that the outer-edge velocity u_e is equal to the piston velocity $U_0(t)$, Eq. (A.1) yields

$$\Gamma_0 = \int_0^{t_0} \frac{1}{2} U_{0(t)}^2\, \mathrm{d}t \tag{A.2}$$

In the case of trapezoidal piston-velocity profiles that were used in the experiments to generate the vortex rings, the integration of Eq. (A.2) results in

$$\Gamma_0 = \frac{1}{6} U_0^2 t_0 [t_{up}^* + 3t_{sl}^* + t_{do}^*]$$

$$\text{with} \quad t_i^* = \frac{t_i}{t_0}, \quad t_{up}^* + t_{sl}^* + t_{do}^* = 1, \tag{A.3}$$

where t_{up} designates the acceleration time, t_{sl} the period of constant velocity U_0, t_{do} the deceleration time, and t_0 the total time of the piston motion.

Following Didden (1979), a velocity-program factor P can be defined that characterizes the shape of the actual piston-velocity profile by normalizing Γ_0 with the circulation $\Gamma_{0,\mathrm{ave}}$ that results from a square function of the piston-velocity average $\bar{U}_0$. For a trapezoidal velocity profile, the circulation $\Gamma_{0,\mathrm{ave}}$ and the velocity program factor are

$$\Gamma_{0,\mathrm{ave}} = \frac{1}{2} \bar{U}_0^2 t_0 = \frac{1}{8} U_0^2 t_0 [t_{up}^* + 2t_{sl}^* + t_{do}^*]^2 \tag{A.4}$$

and

$$P = \frac{\Gamma_0}{\Gamma_{0,\mathrm{ave}}} = \frac{4}{3}\left[1 - \left(\frac{t_{sl}^*}{1 + t_{sl}^*}\right)^2\right] \tag{A.5}$$

For example, it follows from Eq. (A.5), that the velocity-program factor of a square function ($t_{sl}^* = 1$) results in $P = 1$ and of *any* triangular piston motion ($t_{sl}^* = 0$) in $P = 4/3$.

References

Batchelor GK (1967) An introduction to fluid dynamics. Cambridge: University Press

Cantwell BJ; Rott N (1988) The decay of a viscous vortex pair, Phys Fluids 31: 3213–3224

Didden N (1979) On the formation of vortex rings: rolling-up and production of circulation, J Appl Math Phys 30: 101–116

Gharib M; Weigand A; Willert C; Liepmann D (1992) Experimental studies of vortex reconnection to a free surface: a physical flow model, In Proc 19th Symp on Naval Hydrodynamics, Seoul, Korea, National Academic Press, 507–520

Gharib M; Weigand A (1996) Experimental studies of vortex disconnection and connection at a free surface, J Fluid Mech 321: 53–86

Glezer A; Coles D (1990) An experimental study of a turbulent vortex ring, J Fluid Mech 211: 243–283

Hicks (1885) Researches on the theory of vortex rings-Part II, Phil Trans A 176: 725–780

Kambe T; Oshima Y (1975) Generation and decay of viscous vortex rings, J Phys Soc Japan 38: 271–280

Lamb H (1932) Hydrodynamics, New York: Dover

Maxworthy T (1972) The structure and stability of vortex rings, J Fluid Mech 51: 15–32

Maxworthy T (1977) Some experimental studies of vortex rings, J Fluid Mech 81: 465–495

Nitsche M; Krasny R (1994) A numerical study of vortex ring formation at the edge of a circular tube, J Fluid Mech 276: 139–161

Philips OM (1956) The final period of decay of nonhomogeneous turbulence, Proc Camb Phil Soc 52: 135–151

Pullin DI (1979) Vortex ring formation at tube and orifice openings, Phys Fluids 22: 401–403

Saffman PG (1970) The velocity of viscous vortex rings, Stud Appl Math 49: 371–380

Saffman PG (1978) The number of waves on unstable vortex rings, J Fluid Mech 84: 625–639

Saffman PG (1992) Vortex dynamics, University Press, Cambridge

Sallet DW; Widmayer RS (1974) An experimental investigation of laminar and turbulent vortex rings in air, Z Flugwiss 22: 207–215

Shariff K; Leonard A (1992) Vortex rings, Ann Rev Fluid Mech 24: 235–279

Stanaway SK; Cantwell BJ; Spalart PR (1988) A numerical study of viscous vortex rings using a spectral method, NASA Tech Memo 101 041

Thomson W in p. 511 of **Helmholtz H** (1867) On integrals of the hydrodynamical equations, which express vortex-motion, Phil Mag 33 (Series 4): 485–512

Tung C; Ting L (1967) Motion and decay of a viscous vortex ring, Phys Fluids 10: 901–910

Weigand A (1993) The response of a vortex ring to a transient spatial cut, Ph.D. Thesis, University of California, San Diego

Widnall SE; Bliss DB; Tsai CY (1974) The instability of short waves on a vortex ring, J Fluid Mech 66: 35–47

Willert CE; Gharib M (1991) Digital particle image velocimetry, Exp Fluids 10: 181–193